Design and Experimental Verification of a Direct-Drive Interior PM Synchronous Machine Using a Saturable Lumped-Parameter Model*

Edward C. Lovelace
SatCon Technology Corporation
Cambridge, MA, USA
ed.lovelace@satcon.com

Thomas M. Jahns, Jackson Wai
University of Wisconsin-Madison
Madison, WI, USA
jahns@engr.wisc.edu, waij@cae.wisc.edu

Thomas Keim, Jeffrey H. Lang, David D. Wentzloff
Massachusetts Institute of Technology
Cambridge, MA, USA
tkeim@mit.edu, lang@mit.edu, ddw@mit.edu

Franco Leonardi, John M. Miller
Ford Motor Company
Dearborn, MI, USA
fleonar2@ford.com, jmille24@ford.com

Patrick J. McCleer
McCleer Power Inc.
Jackson, MI, USA
pat@mccleerpower.com

***Abstract*— This paper presents the design and experimental verification of a 6kW interior permanent magnet (IPM) synchronous machine intended for an automotive direct-drive starter/alternator application. The machine was designed using a saturable lumped-parameter magnetic circuit model in combination with a Monte Carlo optimization process that minimized the machine-plus-converter cost. An experimental IPM machine has been constructed based on the resulting design specifications. Laboratory tests have confirmed the accuracy of the analytical models for predicting the *q*-axis inductance L_q (including saturation effects) and the torque production characteristics, but discrepancies between the predicted and measured *d*-axis inductance L_d were revealed. The impact of these differences on machine performance is discussed, as well as potential adjustments in the IPM analytical model to improve the performance of future machines.**

Keywords—alternator; generator; interior permanent magnet synchronous machine; lumped parameter model; magnetic saturation; starter.

I. INTRODUCTION

Interior permanent magnet synchronous (IPM) machines are presently being used in a wide variety of commercial, industrial, and transportation applications. However, the nonlinear electromagnetic characteristics of this machine have posed special challenges to designers and discouraged the selection of the IPM machine in some new applications. Previous lumped-parameter models of IPM machines that have been developed to calculate the *d*- and *q*-axis inductances of the IPM salient rotor structure have typically adopted linear models for the magnetic materials without directly including magnetic saturation effects [1-3]. More complex nonlinear models have been used to predict the performance of IPM machines under the assumption of radial flux distribution in the airgap. In [4] the authors recognize that L_q becomes progressively more saturated with loading resulting in a 50 percent reduction at high currents.

This paper is based on recent work that has developed a nonlinear lumped-parameter model (LPM) for the IPM machine that explicitly incorporates the effects of magnetic core saturation along the axis orthogonal to the rotor magnet flux, defined as the *q*-axis [13]. This lumped-parameter model is flexible enough to accommodate many important structural design variations while remaining sufficiently tractable for rapid, repetitive design optimizations. It has been successfully used to evaluate IPM machine designs of various pole numbers and stator slotting distributions. While the analysis focuses on machines with two layers of buried magnets, it can be extended to higher numbers of magnet layers.

One of the prime applications of this saturable LPM approach to date has been the design of an automotive direct-drive starter/alternator (S/A) machine. Fig. 1 shows the cross-section of a single pole in a 12-pole IPM machine designed for this application. Each rotor pole contains two layers of buried magnets that are magnetized across their shorter dimensions along the *d*-axis. The stator of the IPM machine is excited with polyphase balanced sinusoidal currents to produce the characteristic synchronously-rotating mmf wave. Control of

*The research is supported by the MIT Consortium on Advanced Automotive Electrical/Electronic Components and Systems, http://auto.mit.edu/consortium. The experimental IPM machines were built by McCleer Power Inc., Jackson MI, with the financial support of Ford Motor Company. Additional support from the Wisconsin Electric Machines and Power Electronics Consortium (WEMPEC) is also acknowledged.

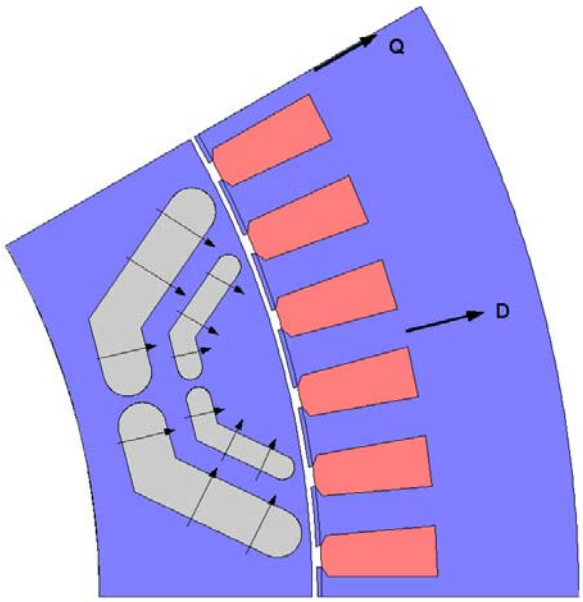

Fig. 1: A single pole cross-section of a 12-pole IPM machine.

torque (motoring) or electrical power output (generating) can be achieved using vector control methods by varying the amplitudes and polarities of the *d*- and *q*-axis currents. The inherent magnetic saliency of the IPM machine makes it possible to apply flux-weakening current excitation along the negative *d*-axis to obtain a wide constant power speed range with appropriately designed machines [7-9].

Although details of this design are presented elsewhere [14], test results from prototype versions of this machine have only recently become available. The purpose of this paper is to present key results from these experimental tests as a means of exploring the strengths and weaknesses of the nonlinear LPM approach, including a comparison to the results of well-known two-dimensional finite element analysis techniques. An additional purpose is to document the performance characteristics of this particular IPM machine design as a candidate for the demanding starter/alternator application.

The paper will begin with a summarized review of the lumped-parameter model in Section II. Key details of the starter/alternator IPM machine design and the prototype machines are presented in Section III, followed by presentation of the experimental results and a comparison with analytical predictions in Section IV. Measured variables include the back-emf, saturable *d*- and *q*-axis inductances, vector-controlled motoring torque, and power generation capability as a function of rotor speed. Measurements of machine efficiency during generating operation are also provided. Finally, conclusions are presented in Section V.

II. Electromagnetic Lumped Parameter Model

Separate lumped parameter equivalent circuit models have been developed for the *d*- and *q*-axes of the IPM machine. The *d*- and *q*-axis inductances are estimated using these circuits as described in a previous paper [13]. First, the *d*-axis inductance L_d is determined from inductance ratios defined with respect to an unsaturated *q*-axis inductance model [1-3]. The piecewise-constant flux amplitude along the airgap is determined from the equivalent magnetic circuit models. This spatial flux distribution is then used to calculate the fundamental component of flux linkage using Fourier analysis, providing the basis for calculating L_d. The fundamental component of the *d*-axis airgap flux linkage under conditions of zero stator current excitation leads directly to the calculated value of λ_{PM} [13].

It is worth pointing out that this model assumes that the *d*-axis magnetic circuit is largely unsaturated because of the magnet cavities that function as large airgaps. The exceptions are the structural rotor bridges and ribs where the iron is fully saturated over a wide range of loads. These structural members link the main pole sections of the rotor core at the air gap to form a unitary lamination.

For the *q*-axis magnetic circuit, a similar approach is followed as for the *d*-axis except that the rotor includes nonlinear saturable reluctance elements that have reluctance values depending on the magnetic flux they are carrying. Iterative calculations are required to solve this nonlinear magnetic circuit, and the resulting fundamental component flux linkage is divided by the *q*-axis current, I_q, to determine the *q*-axis inductance, L_q, as a function of this current amplitude [13-14]. Magnetic cross-coupling between the *d*- and *q*- axes is assumed to be negligible in this LPM model [3, 6].

One of the major objectives of the IPM machine model is to accurately predict the electromagnetic torque produced by the machine using lumped-parameter analysis. The *dq*-frame lumped parameter equation for the electromagnetic torque developed by a three-phase salient-pole synchronous machine is given as follows [10]:

$$T_e = \tfrac{3}{2}\, p\left(\lambda_{PM} - \left(L_q - L_d\right)I_d\right)I_q \qquad (1)$$

where p is the number of pole-pairs, λ_{PM} is the fundamental flux linkage due to the permanent magnets, and the inductances and currents (L_d, L_q, I_d, and I_q) are defined such that the *d*-axis is coincident with the fundamental PM flux axis as shown in Fig. 1. This formula maintains its validity under conditions of magnetic saturation by allowing the inductances to vary as a function of the operating point current conditions, e.g., $L_q = L_q\left(I_q\right)$.

III. Optimized Design & Prototype Construction

A cost-optimized IPM machine design was developed for the 42V automotive starter/alternator application using the saturable lumped parameter model described above [5]. This design was selected based on Monte Carlo optimization techniques using a machine-plus-inverter cost function [14,15].

Experimental IPM machines were then constructed according to the specifications in Table 1 , which closely approximate the optimized design results. The stator laminations were stacked unskewed, and the phase coils were arranged using a single-layer basket-winding configuration. The two magnet cavity layers in each pole were designed with

TABLE 1: IPM MACHINE PARAMETERS.

Design Parameter	Value
Active Length	58 mm
Rotor OD	246 mm
Stator OD	280 mm
Air Gap	0.699 ± 0.025 mm
# Poles	12
# Stator Slots	72
# Magnet Layers Per Pole	2
Core Material	M19, 26 Ga
PM Remanence	>0.28 T
PM Relative Permeability	1.0 to 1.05
Winding Type	Single layer basket
Coil Specifications	19.5 Ga, 13 in-hand
Phase Current at 150 Nm starting torque	327 Arms
Phase Voltage at 6 kW generating power	19.3 Vrms

a central rib along the *d*-axis (see Fig. 1) to provide the necessary mechanical integrity for high-speed operation up to 6000 rpm. Each of the lamination sections around the ends of the cavities is 1 mm wide at the narrowest point. The 96 bonded neodymium-iron rotor magnet pieces were pre-magnetized, inserted, and then potted. Fig. 2 is a photograph of one of three identically constructed machines.

These machines have been tested on similar dynamometer drive stands at Ford Research Laboratory, MIT, University of Wisconsin-Madison, and at McCleer Power. Fig. 3 shows a schematic of the University of Wisconsin-Madison test stand. This drive stand utilizes a four-quadrant induction motor drive as both the prime mover and load coupled to the IPM machine under test. A commercial drive unit has been modified to receive *dq*-current control and voltage commands from a dSPACE DSP system board resident in a PC. The PC records position, current, voltage, and torque feedback data during tests.

Fig. 4 shows a CAD cross-section of the IPM machine installation. The rotor is fit onto an aluminum hub that is designed with an inner bolt circle that is attached to the shaft. An outer bolt circle on an end flange of the hub bolts through the *q*-axis of each pole of the rotor stack. These machines have

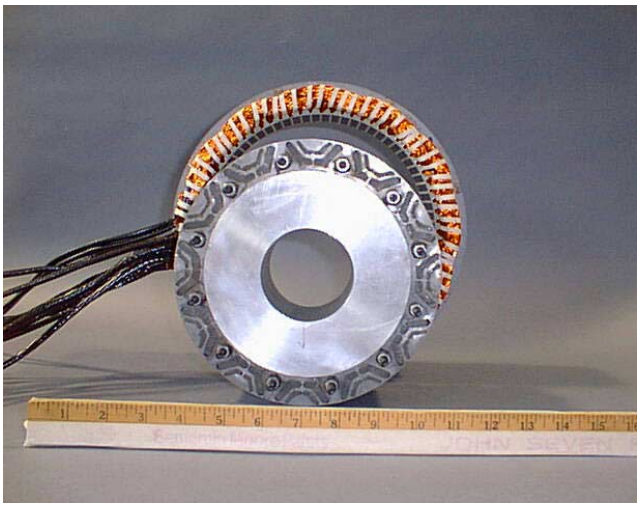

Fig. 2: Photograph of the assembled stator and rotor components.

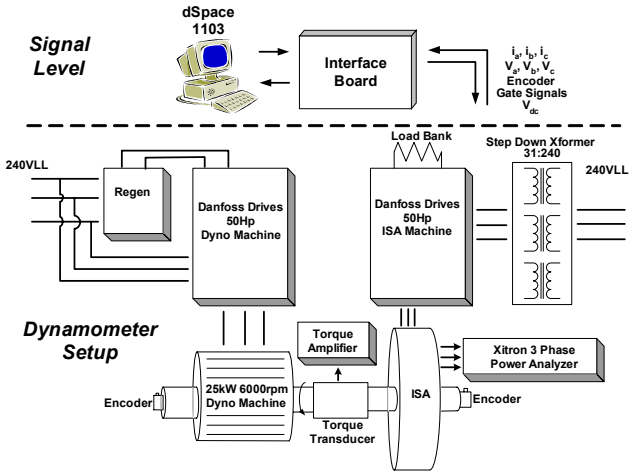

Fig. 3: Schematic of University of Wisconsin-Madison dynamometer test stand.

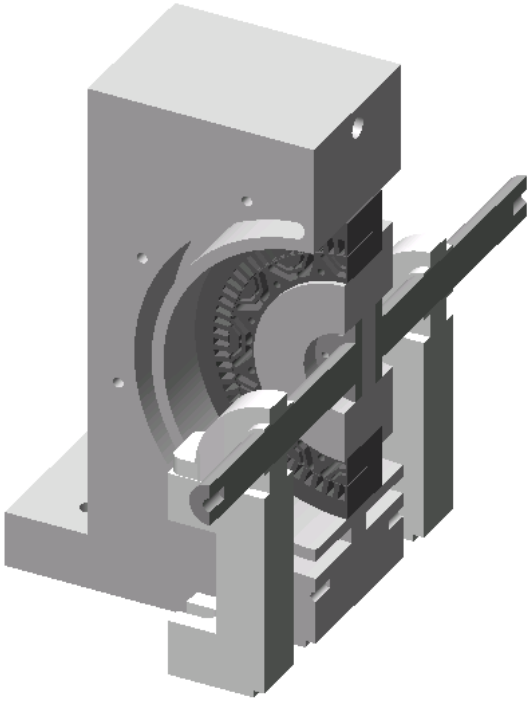

Fig. 4: CAD section of experimental motor, housing, rotor hub, and

been tested at speeds from standstill up to 6000 rpm on test stands at Ford, MIT, and the University of Wisconsin-Madison.

IV. EXPERIMENTAL RESULTS AND COMPARISON TO PREDICTIONS

Experimental measurements have been made to verify the saturable lumped parameter model and to map the machine performance characteristics. It is important to note that all analytical results presented in this section are based on the as-built machine dimensions and parameters summarized in Table 1.

A. *Back-emf Measurements*

The fundamental rms amplitude of the back-emf was measured over the full operating speed range of the machine and compared to the lumped parameter model (LPM) predictions as shown in Fig. 5. The experimental results are linear over this speed range and measured values are approximately 2.5% lower than predicted using these as-built parameters. Two-dimensional finite element analysis (FEA)[1] predictions are 7.2% higher than the LPM predictions. Fig. 6 shows a time trace of the measured open-circuit phase voltage at 6000 rpm, together with the extracted fundamental component.

B. L_q *Measurements*

Fig. 7 shows a comparison of L_q predictions using the as-built machine parameters resulting from the LPM and 2D FEA, compared with independent experimental measurements at three locations. Since the 2D FEA cannot model end turn leakage, the value predicted by the LPM is added as a post-processing step and included in the plotted FEA results. L_q, particularly at low current levels, is relatively sensitive to the precise airgap length, so the 2D FEA was executed at both airgap measurement precision extremes (see TABLE 1) and the results are represented as vertical error bars on the nominal FEA result in Fig. 7. Comparison of the LPM and FEA results suggests that the LPM is probably overestimating the in-plane leakage components (i.e., other than end-turn leakage) by 10 μH due to the nearly constant offset between the two predicted curves.

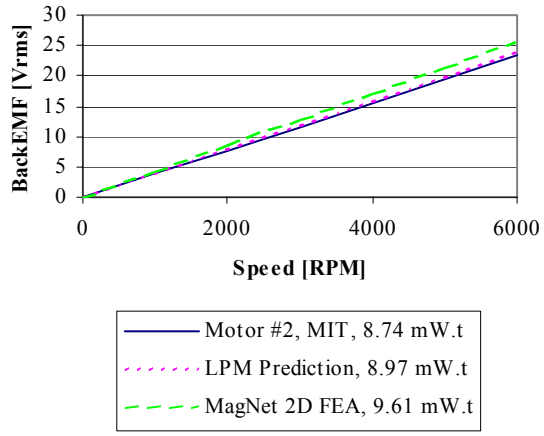

Fig. 5: Experimental verification of back emf over full speed range.

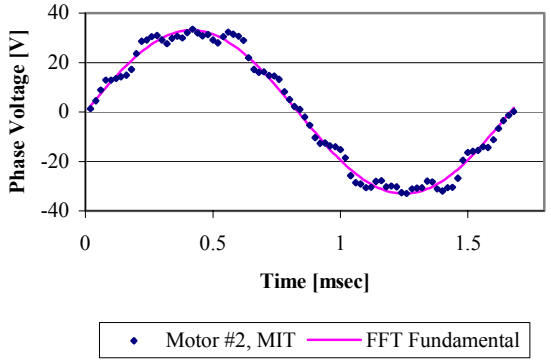

Fig. 6: Measured open circuit terminal voltage at 6000 rpm.

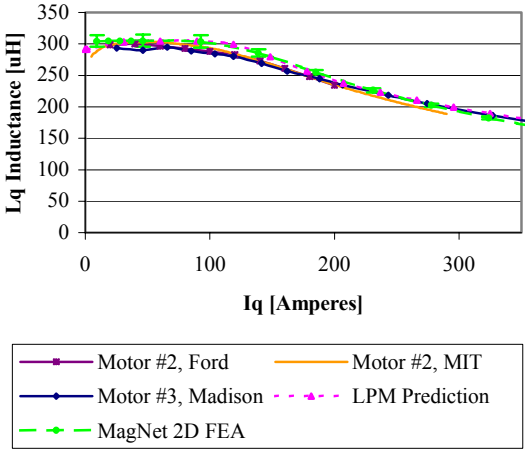

Fig. 7: Comparison of *Lq* experimental measurements, lumped parameter model (LPM) predictions, and 2D FEA results.

The experimental L_q measurements in Fig. 7 were developed using two methods. According to the first approach, the rotor is locked at a known angle with respect to the stator, and the machine is excited along the rotor's *q*-axis (i.e., $I_d = 0$) using single-phase 60 Hz ac excitation in order to collect voltage and current impedance data. For the second approach, the machine is operated at low speed under current-regulated vector control with only *q*-axis current excitation, and the resulting *d*-axis voltage measurements ($V_d = \omega\lambda_q = \omega L_q I_q$ for $I_d = 0$) are used to calculate L_q.

The plot of L_q as a function of *q*-axis current I_q in Fig. 7 demonstrates very good agreement between predictions and experimental measurements over the full range of current values, confirming the validity of the saturable lumped-parameter model for L_q. Residual differences between the measured and predicted values at low values of I_q (< 20A) are relatively insignificant in terms of machine performance and may be caused by inaccuracies in the analytical model of the iron permeability at low flux density levels, or measurement inaccuracies at low voltage and current signal levels. Sensitivity studies using 2D FEA have indicated that L_q is insensitive to other factors such as the PM material properties and stator slot ripple.

C. L_d *Measurements*

Fig. 8 shows the comparison of L_d measurements and predictions using the same measurement approaches described above for L_q. Note that the polarity of the I_d current is imposed in the negative direction to achieve the highest possible torque-per-Amp in this type of machine. Negative

[1] MagNet v6.10.1, Infolytica Corporation, Montreal, CANADA, 2002.

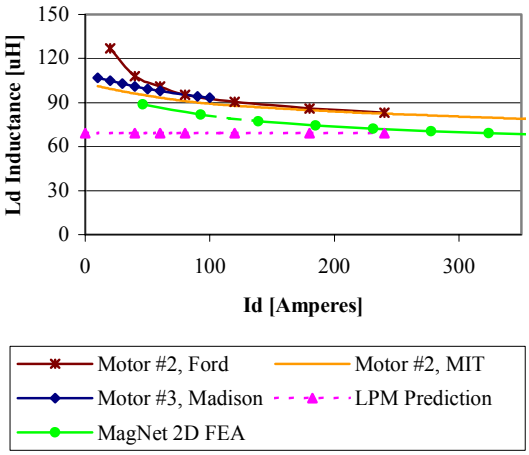

Fig. 8: Comparison of Ld experimental measurements, lumped parameter model (LPM) predictions, and 2D FEA results.

values of I_d also act to reduce (weaken) the total *d*-axis flux linkage λ_d while simultaneously increasing the level of magnetic saturation in the rotor lamination bridges surrounding the ends of the magnet cavities.

The measured values of L_d are extracted from the voltage and current measurements using the same techniques described above for L_q except that the value of the magnet flux linkage λ_{PM} must be subtracted first from the *d*-axis flux linkage value λ_d as a DC offset (i.e., $V_q = \omega\lambda_d = \omega(L_d I_d + \lambda_{PM})$ for $I_q = 0$) before calculating L_d. It should be noted that the magnet flux linkage λ_{PM} is assumed to be a constant value for all values of *d*- and *q*-axis stator current. The measured value of L_d is particularly sensitive to errors in λ_{PM} at low values of I_d.

One of the characteristics of the adopted lumped parameter model is that the value of L_d is assumed to be constant for all values of I_d, based on a simplified assumption that the lamination bridges remain fully saturated at all *d*-axis current amplitudes down to zero. However, examination of the 2D FEA results in Fig. 8 reveals that these bridges are not fully saturated at low I_d amplitudes, so that the value of L_d predicted by 2D FEA exceeds the LPM prediction when the *d*-axis current is low. Note that the measured value of L_d gradually approaches the LPM prediction at high values of I_d.

In addition to this difference between FEA and LPM predictions for L_d, Fig. 8 reveals that the measured values of L_d collected from all three dynamometer test sites are notably higher than the predicted values from either analytical approach. The shapes of the measured L_d characteristics parallel those of the 2D FEA predictions, but they are offset by approximately 10 µH above the predicted values over a wide range of I_d current amplitudes greater than approximately 50 A. At high current amplitudes, the LPM prediction is at least 13 µH lower than the experimental measurement calculations.

As a result of these differences, the measured L_d values exceed the constant LPM prediction by at least 35% at $I_d = 50$A, and by approximately 20% at 240A. (The cause of the fast-rising L_d values for low I_d with one of the measured curves in this figure labeled Motor #2, Ford is not fully understood, but may be caused by the sensitivity to errors in λ_{PM} noted above.)

There are several factors that may be contributing to the discrepancies between predicted and measured L_d values. These factors include stator slot ripple caused by the unskewed stator, three-dimensional magnetic fringing flux, core and magnet B-H permeability properties, and rotor bridge geometry. While some of these factors are subject to manufacturing uncertainties, others such as the slot ripple and fringing flux are candidates for analytical investigations. Fig. 9 provides the results of 2D FEA showing that the value of L_d varies by approximately 9% due to slot ripple as the rotor is rotated through two slot pitches with constant amplitude and vector orientation of the stator current along the rotor *d*-axis ($I_d = 462$ A). This variation in L_d contributes a torque ripple component at the slot frequency (72 slots per revolution), and the impact of this variation on the comparison between predicted and measured L_d values in Fig. 9 is presently being evaluated.

Since this particular IPM machine has a short active core length compared to its diameter, the effects of magnetic fringing flux from the ends of the rotor stack around the magnet cavities deserves closer consideration in view of the L_d discrepancies. Although a three-dimensional FEA has not yet been carried out, approximate calculations of the fringing effects based of established magnetic circuit approximations [17] indicate that the inclusion of the fringing flux effects will raise the predicted L_d value by at least 8%. Although this is not enough to account for the entire discrepancy, it appears to be a significant contributing factor.

Taken together, these results suggest that a combination of factors is responsible for causing the low prediction of the machine *d*-axis inductance, and that more work is necessary to properly account for these additional factors in future IPM machine designs.

D. *Torque vs. Angle Measurements*

Fig. 10 shows several static torque curves for the IPM

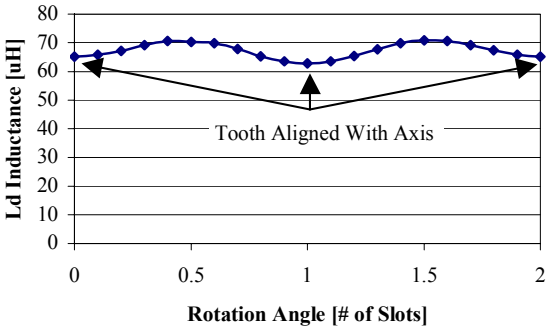

Fig. 9: 2D FEA showing Ld sensitivity to stator slot position (*Id*= 327 Arms).

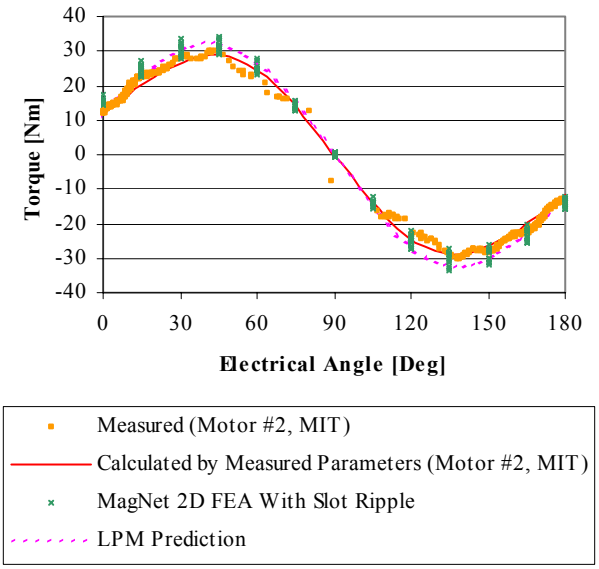

Fig. 10: Torque vs. control angle γ comparisons (*Ia*=150 Adc).

machine plotted versus current orientation angle γ, comparing measurements and predictions for a fixed current amplitude of 150 A. (Angle γ is defined positive in the counterclockwise direction with respect to the positive *q*-axis.) The data is presented over the range from γ = 0 to 180 electrical degrees corresponding to the 2nd (motoring) and 3rd (generating) *dq*-plane quadrants for which I_d is always negative ($I_q = 0$ at γ = 90 deg).

The major role of the reluctance torque in this machine's torque production characteristics is apparent in the shape of the Fig. 9 torque curves that are dominated by a (sin 2γ) component. The measured torque values agree quite closely with the predicted torque values that were calculated using Eqn. 1 and the measured machine parameters.

The 2D FEA torque results show the effects of stator slot ripple by plotting a family of calculated torque values for different stator slot positions at each γ angle that captures the minimum and maximum torque values. For the 150 A current excitation conditions used in Fig. 10, the peak-to-peak torque ripple at the peaks of the torque curve corresponds to approximately 17% of the average torque values. This significant ripple component illustrates the importance of design techniques such as skewing of either the stator or rotor lamination stacks in order to minimize this undesirable torque ripple effect. The spacing of the magnet cavities in comparison to the stator slot pitch also deserves careful attention in order to minimize ripple torque production.

E. Torque and Power vs. Speed Measurements

Fig. 11 and 12 present curves for the maximum torque and power envelopes, respectively, for the starter/alternator IPM machine as a function of rotor speed. The measured torque-speed curve in Fig. 11 corresponds to motoring operation with the stator excitation limited by a 42 Vdc bus (i.e., approximately 18.9 Vrms per phase). Differences between the predicted envelope using measured parameters and the

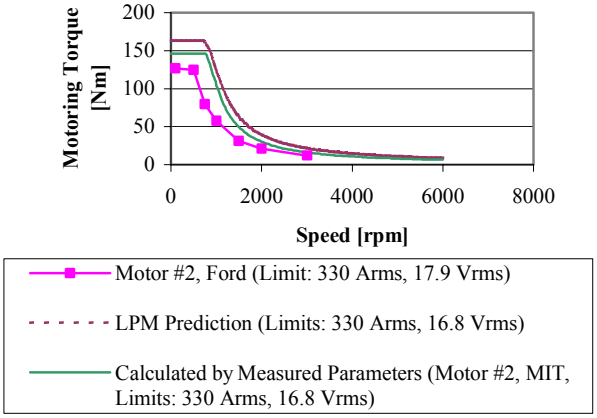

Fig. 11: Motoring torque vs. speed measurements and predictions.

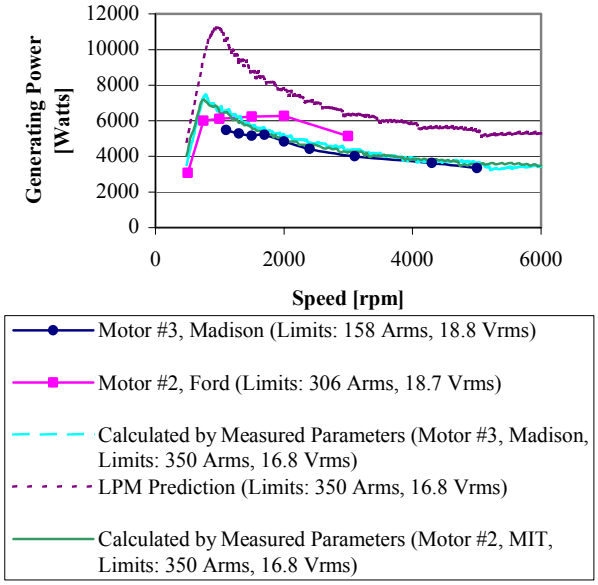

Fig. 12: Comparison of power generation measurements and predictions.

measured data (146 Nm vs. 125 Nm maximum torque at 330 Arms) are being investigated further.

The power-speed capability curve in Fig. 12 for generating operation is compared to calculated envelope curves from measured parameters and LPM predictions based on as-built machine dimensions. This figure shows that the measured maximum power generation capability starts to fall off above 3000 rev/min, dropping approximately 33% below the high-speed power envelope predicted by the LPM analysis. The measured power generation data from Ford and Madison agree quite well with differences due to the individual inverter characteristics and imposed voltage limits as noted.

Sensitivity calculations have indicated that the high-speed torque/power envelope difference is caused primarily by the discrepancy between measured and LPM-predicted L_d values that was discussed previously. This observation is corroborated by the fact that the predicted and measured envelope curves agree quite closely when the measured machine parameters including L_d variations with I_d are used to develop the envelope predictions.

These results highlight that the high-speed power capabilities of the IPM machine are quite sensitive to errors in the value of L_d, emphasizing the importance of improvements in this portion of the LPM design approach.

F. *Measured Machine Efficiency*

Fig. 13 shows measurements of the machine efficiency during generator operation as a function of the rotor speed for load operating points along the maximum power/torque envelopes in Figs. 11 and 12. These curves were calculated using voltage and current measurements at the terminals of the machine, eliminating converter losses from the machine efficiency calculations.

The Madison measurements show that the IPM machine efficiency peaks at 85 to 90% for typical cruise engine speeds (1500 to 2500 rev/min). The drop in machine efficiency at high speeds suggests that frequency-sensitive loss components such as iron losses deserve closer attention. This investigation will determine what steps can be taken to both improve the loss performance prediction accuracy in this high-speed range, as well as to reduce the amount of IPM machine losses at high rotational speeds. The Ford data, which was collected at higher current loads up to 306 Arms, shows a characteristic decrease in efficiency peaking at 82% for 6 kW, 1500 rev/min.

V. CONCLUSIONS

Key observations and conclusions that can be derived from the results presented in this paper include the following:

- Experimental tests with the IPM S/A machine confirm that the nonlinear lumped parameter model is capable of providing accurate estimates of the highly saturable L_q parameter and the PM flux linkage λ_{PM}, but that a more sophisticated model is desirable for L_d predictions.
- The present LPM model is capable of predicting low-speed operating characteristics including torque production and voltage-current characteristics quite well, but the prediction of the high-speed maximum power-speed envelope can be quite sensitive to any L_d discrepancies.
- Closer examination has revealed that L_d is sensitive to a variety of electromagnetic effects caused by stator slot ripple, rotor bridge dimensions, and magnetic flux fringing at the stack ends (particularly for short rotors) that complicate accurate prediction of L_d.

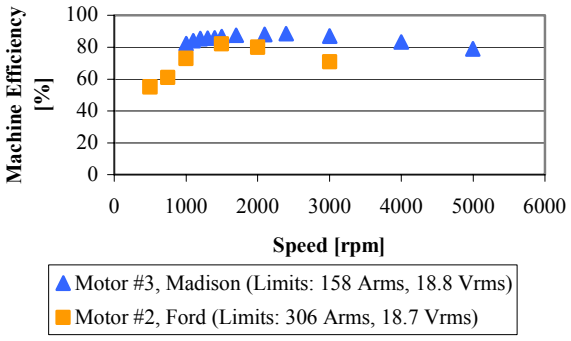

Fig. 13: Measured max generating load machine efficiency.

Additional tests are now being conducted with the IPM S/A machine to more fully document its nonlinear operating characteristics and to understand the strengths and limitations of the existing analytical tools for predicting them. This investigation is providing the basis for developing the necessary modifications to improve the predictive accuracy of the LPM and FEA techniques. These improved analytical tools will play a key role in developing future IPM machine designs that will meet their performance requirements under all operating conditions, including the particularly demanding regime of high-speed constant power operation.

REFERENCES

[1] A. Fratta, A. Vagati, and F. Villata, "Design Criteria of an IPM Machine Suitable for Field-Weakened Operation," in Proc. Intl. Conf. on Elec. Machines, 1990, pp. 1059-1065.

[2] T. A. Lipo, T. J. E. Miller, A. Vagati, I. Boldea, L. Malesani, and T. Fukao, "Synchronous Reluctance Drives Tutorial," presented at IEEE IAS Annual Meeting, 1994.

[3] A. Vagati, A. Fratta, G. Franceschini, and P. M. Rosso, "A.C. Motors for High-Performance Drives: A Design-Based Comparison," in Proc. IEEE IAS Annual Meeting, 1995, pp. 725-733.

[4] E. Richter, T.W. Neumann, "Saturation Effects in Salient Pole Synchronous Motors with Permanent Magnet Excitation," International Conference on Electrical Machines, Proceedings Part 2, pgs 603-606, Lausanne, Switzerland, 18-21 Sept. 1984

[5] E. C. Lovelace, T. M. Jahns, J. L. Kirtley Jr., and J. H. Lang, "An Interior PM Starter/Alternator for Automotive Applications," in Proc. ICEM, Istanbul, 1998, vol. 3, pp. 1802-1808.

[6] A. Vagati, M. Pastorelli, and G. Franceschini, "Effect of Magnetic Cross-coupling in Synchronous Reluctance Motors," in Proc. Intelligent Motion, 1997, pp. 279-285.

[7] R. Schiferl and T. A. Lipo, "Power capability of salient pole P.M. synchronous motors in variable speed drive," in Proc. IEEE-IAS Annual Meeting, 1988, pp. 23-31.

[8] T. M. Jahns, "Flux Weakening Regime Operation of an IPM Synchronous Motor Drive," IEEE Transactions on Industry Applications, vol. IA-23, pp. 681-689, 1987.

[9] W. L. Soong and T. J. E. Miller, "Field-Weakening Performance of Brushless Synchronous AC Motor Drives," IEE Proceedings - Elec. Power Appl., vol. 141, pp. 331-339, 1994.

[10] T. J. E. Miller, Brushless Permanent-Magnet and Reluctance Motor Drives. Oxford: Clarendon Press, 1989.

[11] W. Soong, "Design and Modelling of Axially-Laminated Interior Permanent Magnet Motor Drives for Field-Weakening Applications," Ph.D. Thesis in Department of Electronics and Electrical Engineering: University of Glasgow, 1993.

[12] I. Boldea, Reluctance Synchronous Machines and Drives. Oxford: Clarendon Press, 1996.

[13] E. C. Lovelace, T. M. Jahns, and J. H. Lang, "A Saturating Lumped Parameter Model for an Interior PM Synchronous Machine," IEEE Trans. Ind. Appl., vol. 38, pp. 645-650, May/June 2002.

[14] E. C. Lovelace, " Optimization Of A Magnetically Saturable Interior Permanent-Magnet Synchronous Machine Drive", Ph.D. Thesis, Department of Electrical Engineering and Computer Science, Massachusetts Institute of Technology, May 2000.

[15] E. C. Lovelace, T. M. Jahns, and J. H. Lang, "Impact of Saturation and Inverter Cost On Interior PM Synchronous Machine Drive Optimization," IEEE Trans. on Industry Applications, vol. IA-36, pp. 723-729, May/June, 2000.

[16] R. Schiferl, T.A. Lipo, "Core Loss in Buried Magnet Permanent Magnet Synchronous Motors," IEEE Transactions on Energy Conversion, Vol. 4, No. 2, pgs 279-284, June 1989.

[17] H.C. Roters, Electromagnetic Devices, J. Wiley & Sons, New York, 1941.